



Variability and properties of liquid-dominated clouds over the ice-free and sea-ice-covered Arctic Ocean

Marcus Klingebiel¹, André Ehrlich¹, Elena Ruiz-Donoso¹, Nils Risse², Imke Schirmacher², Evelyn Jäkel¹, Michael Schäfer¹, Kevin Wolf⁵, Mario Mech², Manuel Moser^{3,4}, Christiane Voigt^{3,4}, and Manfred Wendisch¹

¹Leipziger Institut für Meteorologie (LIM), Universität Leipzig, Leipzig, Germany

²Institut für Geophysik und Meteorologie (IGM), Universität zu Köln, Cologne, Germany

³Institut für Physik der Atmosphäre, Deutsches Zentrum für Luft- und Raumfahrt, Wessling, Germany

⁴Institut für Physik der Atmosphäre, Johannes Gutenberg-Universität, Mainz, Germany

⁵Institut Pierre-Simon Laplace, Sorbonne Université/CNRS, Paris, France

Correspondence: Marcus Klingebiel (marcus.klingebiel@uni-leipzig.de)

Received: 20 December 2022 – Discussion started: 6 January 2023

Revised: 13 October 2023 – Accepted: 24 October 2023 – Published: 14 December 2023

Abstract. Due to their potential to either warm or cool the surface, liquid-phase clouds and their interaction with the ice-free and sea-ice-covered ocean largely determine the energy budget and surface temperature in the Arctic. Here, we use airborne measurements of solar spectral cloud reflectivity obtained during the Arctic CLOUD Observations Using airborne measurements during polar Day (ACLOUD) campaign in summer 2017 and the Arctic Amplification: FLUXes in the Cloudy Atmospheric Boundary Layer (AFLUX) campaign in spring 2019 in the vicinity of Svalbard to retrieve microphysical properties of liquid-phase clouds. The retrieval was tailored to provide consistent results over sea-ice and open-ocean surfaces. Clouds including ice crystals that significantly bias the retrieval results were filtered from the analysis. A comparison with in situ measurements shows good agreement with the retrieved effective radii and an overestimation of the liquid water path and reduced agreement for boundary-layer clouds with varying fractions of ice water content. Considering these limitations, retrieved microphysical properties of clouds observed over the ice-free ocean and sea ice in spring and early summer in the Arctic are compared. In early summer, the liquid-phase clouds have a larger median effective radius (9.5 μm), optical thickness (11.8) and effective liquid water path (72.3 g m^{-2}) compared to spring conditions (8.7 μm , 8.3 and 51.8 g m^{-2} , respectively). The results show larger cloud droplets over the ice-free Arctic Ocean compared to sea ice in spring and early summer caused mainly by the temperature differences in the surfaces and related convection processes. Due to their larger droplet sizes, the liquid clouds over the ice-free ocean have slightly reduced optical thicknesses and lower liquid water contents compared to the sea-ice surface conditions. The comprehensive dataset on microphysical properties of Arctic liquid-phase clouds is publicly available and could, e.g., help to constrain models or be used to investigate effects of liquid-phase clouds on the radiation budget.

1 Introduction

Over the past 3 decades, the Arctic region has experienced enhanced warming, which exceeds global warming by a factor of 2 to 4 (Serreze and Francis, 2006; Serreze and Barry, 2011; Wendisch et al., 2017; Rantanen et al., 2022). This resulted in a drastic decrease in the Arctic sea-ice extent (e.g., Stroeve et al., 2012), which changes the surface en-

ergy budget and surface fluxes of heat and moisture. The intertwined processes and feedback mechanisms behind these and further rapid changes in the Arctic climate system are widely referred to as Arctic amplification (Wendisch et al., 2017, 2022). To investigate and better understand the causes, i.e., the involved key processes and major feedback mechanisms, and effects of Arctic amplification, the Transregional

Collaborative Research Center called Arctic Amplification: Climate Relevant Atmospheric and Surface Processes and Feedback Mechanisms ((AC)³, <http://www.ac3-tr.de>, last access: 6 December 2023) was initiated.

Within the framework of (AC)³, several field studies were conducted to cover a variety of spatial and temporal scales. In this study, we focus on the airborne campaigns Arctic CLOUD Observations Using airborne measurements during polar Day (ACLOUD, May/June 2017, Wendisch et al., 2019) and Arctic Amplification: FLUXes in the Cloudy Atmospheric Boundary Layer (AFLUX, March/April 2019, Mech et al., 2022b), which were performed to study the development of boundary-layer clouds over the sea-ice-covered and ice-free Arctic Ocean. These clouds are often mixed-phase clouds and are suspected of being one of the important factors that contribute to Arctic amplification (Serreze and Barry, 2011) because the partitioning between liquid water droplets and ice crystals within these clouds determines their radiative properties and life cycles (Tan and Storelvmo, 2019).

Commonly, two methods are used to measure the properties of boundary-layer cloud particles from aircraft: first, to sample them directly with in situ instruments, which has the advantage that the size and shape of individual cloud particles can be measured and the accuracy of the instrument can be estimated by a prior calibration; second, to use passive or active remote-sensing measurements to retrieve the cloud properties. In contrast to in situ sampling, remote-sensing observations cover a larger measurement area. However, the information retrieved from passive remote sensing using reflectances is often dominated by the cloud top properties (Platnick, 2000). Unfortunately, passive remote-sensing retrieval from reflectances of Arctic boundary-layer clouds is challenging due to the unknown vertical distribution of ice particles in the typically liquid-dominated clouds (Ruiz-Donoso et al., 2020) and the changing surface albedo differences (i.e., ice-free ocean, sea ice or snow). Liu et al. (2010) and Ehrlich et al. (2017) showed that the surface albedo and surface emissivity differences between the ice-free ocean and sea ice influence the detection of clouds with passive remote-sensing measurements. They compared results from MODIS (passive remote sensing) and CloudSat or CALIPSO (active remote sensing) and found that cloud amount trends in the Arctic show potential differences of up to 3 % per decade. The reason for that is partly the small difference in emissivity between clouds and sea ice, which often leads to the misclassification of thin clouds as sea ice.

In this study, we apply a retrieval method of cloud properties which is based on the bispectral method proposed by Nakajima and King (1990) and Ruiz-Donoso et al. (2020) to identify the properties of boundary-layer clouds over Arctic sea ice and the ice-free ocean. To minimize the uncertainty of the retrieval method, only liquid-dominated clouds are analyzed, which were filtered using the slope phase index parameter (Ehrlich et al., 2008). The cloud properties derived over sea ice from the bispectral retrieval method suffer from

the uncertainties of the assumed sea-ice albedo (e.g., Ehrlich et al., 2017). To reduce this uncertainty, this study makes use of airborne measurements of sea-ice albedo conducted within the campaign, which represent the regional and seasonal sea-ice conditions as closely as possible. Comparing clouds over the ice-free Arctic Ocean and sea ice gives an impression of how cloud properties could change in a future ice-free Arctic summer.

The paper is structured as follows: Sect. 2 introduces the remote-sensing and in situ instruments. In Sect. 3, we present the retrieval method. Section 4 compares the retrieved microphysical properties and in situ measurements. Section 5 shows the differences in the cloud properties over the ice-free ocean and sea ice of the ACLOUD and AFLUX campaigns, followed by a discussion of the results.

2 Aircraft instrumentation

During the summer campaign, ACLOUD, and the spring campaign, AFLUX, airborne measurements with the *Polar 5* research aircraft (Wesche et al., 2016) were conducted. The *Polar 5* flight tracks of both campaigns are presented in Fig. 1. The aircraft was equipped with a set of passive and active remote-sensing instruments as summarized in Ehrlich et al. (2019). Dropsondes were released to deliver vertical profiles of atmospheric parameters. Figure 2 shows the averaged temperature profiles of all launched dropsondes for both campaigns, separated in measurements over sea ice and open ocean. During AFLUX, cloud probes for in situ measurements complemented the setup on *Polar 5*, while for ACLOUD these measurements were performed with a second aircraft.

2.1 Spectral Modular Airborne Radiation measurement system (SMART) albedometer

SMART is configured to measure upward and downward spectral solar irradiance from which the albedo in-flight altitude is derived. For this purpose, optical inlets are mounted on actively stabilized platforms (Wendisch et al., 2019) and connected via optical fibers to grating spectrometers. The upward and downward irradiance, F_{λ}^{\downarrow} , is measured in a spectral range between 300 and 2300 nm with a frequency of 2 Hz and an uncertainty of 8 % (Bierwirth et al., 2013; Wendisch et al., 2019; Ehrlich et al., 2019).

2.2 Airborne Imaging Spectrometer for Applications (AISA) Hawk spectral imager

The AISA Hawk instrument (Ruiz-Donoso et al., 2020; Ehrlich et al., 2019) consists of a downward-viewing push-broom sensor aligned across the flight track to measure 2D fields of upward radiance. The push-broom sensor contains 384 across-track pixels, where each pixel performs

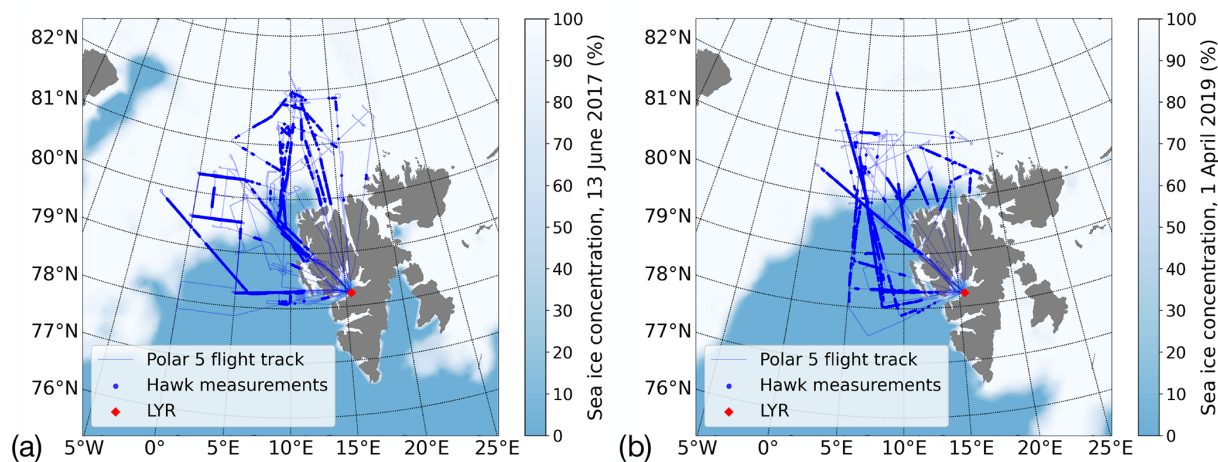


Figure 1. Flight tracks of *Polar 5* during the ACLOUD (a) and AFLUX (b) campaigns in the vicinity of Svalbard, including Longyearbyen airport (LYR) and the flight sections when the AISA Hawk instrument was measuring. The sea-ice concentration is based on the AMSR-E and AMSR2 datasets (Spreen et al., 2008).

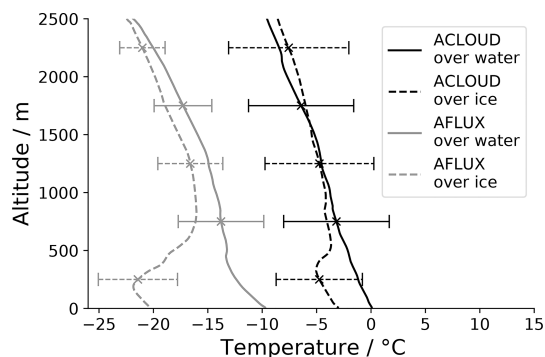


Figure 2. Averaged temperature profiles of all launched dropsondes during the ACLOUD (black) and AFLUX (gray) campaigns over water (continuous lines) and the ice surface (dashed). The horizontal bars represent the standard deviation.

spectral measurements between 930 and 2550 nm wavelength in 288 channels. With a 36° field of view (FOV) and a sampling frequency of 20 Hz, the instrument has a spatial resolution of 2 m assuming a distance of 1 km between aircraft and cloud (Ruiz-Donoso et al., 2020). The flight tracks with the locations of the measurements from the AISA Hawk spectral imager during the summer (ACLOUD) and spring (AFLUX) campaigns are displayed in Fig. 1. Due to storage capacities, AISA Hawk data are only recorded when clouds are present below the aircraft. The uncertainty of the measured radiance is approximately 6 % (Schäfer et al., 2013; Ruiz-Donoso et al., 2020).

The spectral reflectivity, R_λ , is calculated by using the upward radiance measurements, I_λ^\uparrow , from the AISA Hawk spectral imager combined with the downward spectral irradiance, F_λ^\downarrow , measurements from the SMART albedometer:

$$R_\lambda = \pi \cdot \frac{I_\lambda^\uparrow}{F_\lambda^\downarrow}. \quad (1)$$

However, during the AFLUX campaign, condensation on the inside of the optics or an improperly working stabilization platform made the downward radiance and irradiance measurements unreliable. For this reason, the SMART measurements during AFLUX are replaced by simulations of F_λ^\downarrow , which were performed with the Library of Radiative transfer (libRadtran) code (Mayer and Kylling, 2005; Emde et al., 2016). According to Ehrlich et al. (2023), the accuracy of downward simulations is high as atmospheric conditions measured by radiosondes (Ny-Ålesund) and aerosol optical depth (airborne sun photometer) were implemented in the simulations. Within libRadtran we used the radiative transfer solver DISORT2 (Discrete Ordinate Radiative Transfer, Stamnes et al., 2000) and performed the simulations of the upward radiance for solar zenith angles between 55 and 69° . Azimuth angles were adjusted depending on the measurement time, location and attitude of the research aircraft.

Based on R_λ , we calculate the slope phase index, PI,

$$\text{PI} = 100 \cdot \frac{(\lambda_b - \lambda_a)}{R_{1640}} \left(\frac{dR_\lambda}{d\lambda} \right)_{[\lambda_a, \lambda_b]}, \quad (2)$$

for the spectral reflectivity range between $\lambda_a = 1550$ nm and $\lambda_b = 1700$ nm. For typical Arctic conditions, a threshold of $\text{PI} < 20$ serves as an indicator to identify liquid water clouds and exclude mixed-phase and ice clouds from the analysis when required (Ehrlich et al., 2008). The PI is most sensitive to the number of ice crystals and liquid water droplets close to the cloud top. Therefore, the clouds identified by the threshold of $\text{PI} < 20$ need to be considered liquid-dominated clouds.

2.3 Microwave Radar/radiometer for Arctic Clouds (MiRAC) radar

MiRAC combines a frequency-modulated continuous-wave (FMCW) radar at 94 GHz including a 89 GHz passive channel (MiRAC-A) and an eight-channel radiometer with frequencies between 175 and 340 GHz (MiRAC-P, Mech et al., 2019). MiRAC is mounted at the bottom of the fuselage of *Polar 5* with inclinations of $\sim 25^\circ$ (MiRAC-A) and 0° (MiRAC-P) to study low-level, Arctic mixed-phase clouds. The FMCW radar delivers vertically resolved profiles of equivalent radar reflectivity (Kliesch and Mech, 2019; Mech et al., 2022b) for the ALOUD and AFLUX campaigns.

2.4 In situ cloud particle instruments

During AFLUX, *Polar 5* was equipped with an advanced particle measurement configuration including scattering and optical array probes. The Cloud Aerosol Spectrometer (CAS) uses forward-scattered laser light ($4\text{--}12^\circ$, given by the manufacturer) to estimate the cloud droplet size distributions in a diameter size range between 2.8 and 50 μm based on Mie theory (Wendisch and Brenguier, 2013; Klingebiel et al., 2015; Voigt et al., 2017; Kleine et al., 2018; Voigt et al., 2022). Shadow images of hydrometeors are recorded by two optical array probes, the Cloud Imaging Probe (CIP) and the Precipitation Imaging Probe (PIP, Baumgardner et al., 2001; Klingebiel et al., 2015). Both imaging probes differ in pixel resolution, which results in two different ranges for particle size detection (CIP: observable size range from 15 to 960 μm ; PIP: observable size range from 100 to 6400 μm). With a combined particle size distribution from all three instruments (CAS, CIP and PIP), microphysical cloud properties including the effective radius, r_{eff} , the liquid water content (LWC) and the ice water content (IWC) are calculated. In this study, the r_{eff} calculation is based on all observable cloud particle sizes, the LWC is calculated using particles smaller than 50 μm (CAS data), and the IWC is calculated using particles larger than 50 μm (CIP and PIP), which is appropriate for Arctic mixed-phase clouds (McFarquhar et al., 2007; Korolev et al., 2017). Uncertainties of in situ cloud measurements strongly depend on the microphysical cloud properties. In liquid clouds, the droplets are sized by the CAS, which has a range of 10 %–50 % uncertainty (Baumgardner et al., 2017), while in ice and mixed-phase clouds the sizing is dominated by data from the optical array probes, which have an uncertainty of 20 % (Baumgardner et al., 2017; Gurganus and Lawson, 2018). In stratiform liquid and mixed-phase clouds, the calculation of the LWC is subject to an error of 20 % (Faber et al., 2018), and for the IWC, an error of 50 % (Heymsfield et al., 2010; Hogan et al., 2012) is assumed. For the in situ data used here, a description of the processing methods and the derivation of microphysical cloud properties is given in detail by Mech et al. (2022a) and Moser et al. (2023).

3 Retrieval method and design

Cloud microphysical and optical parameters (effective radius, r_{eff} , effective liquid water path, LWP_{eff} , and cloud optical thickness, τ) are retrieved from the AISA Hawk and SMART measurements on the *Polar 5* aircraft in combination with forward radiative transfer simulations to generate look-up tables of cloud top reflectivity. The design and limits of the retrieval are demonstrated in the following.

The radiative transfer simulations are performed with the library for Radiative transfer (libRadtran) code from Mayer and Kylling (2005) and Emde et al. (2016) using the radiative transfer solver DISORT2 (Stamnes et al., 2000). Solar zenith angles (72 to 82° during AFLUX and 55 to 69° during ALOUD, according to Wendisch et al., 2023) and azimuth angles were adjusted for each simulation, depending on the location, altitude and measurement time of the aircraft.

Due to the low contrast between clouds and bright sea-ice surfaces at visible wavelengths, bispectral cloud retrievals typically use measurements at wavelengths larger than 1000 nm (Platnick et al., 2016). For the retrieval method presented here, the reflectivities at 1650 and 2100 nm are applied. Following the approach by, e.g., Ehrlich et al. (2017) or Ruiz-Donoso et al. (2020), the reflectivity at 2100 nm is normalized to a spectral ratio R_{ratio} . To match the observed cloud reflectivities, an appropriate estimate of the surface albedo in the radiative transfer simulations is required.

As shown by Ehrlich et al. (2017), an incorrectly assumed surface albedo can bias the retrieval significantly (Fricke et al., 2014; Platnick, 2001). This holds especially for sea ice, where the surface albedo may change due to different snow grain sizes, leads and melt ponds (Jäkel et al., 2019b, 2021). The albedo measurement was obtained under cloud-free conditions. Because interactions between clouds and surface albedo have to be considered, the measurements cannot be applied directly in the radiative transfer simulations. Instead, a parametrization of the snow albedo for cloudy conditions depending on the snow grain size is used. To identify which snow grain size represents the ALOUD conditions, airborne measurements of snow albedo obtained from low-level flights (5 June 2017) are used. The albedo averaged for the marginal sea-ice zone (MIZ, black line) and pure ice (dotted line) is shown in Fig. 3 and is compared to theoretical snow albedo derived from the snow albedo model by Zege et al. (2011) for different snow grain sizes, assuming a homogeneous snow profile. It is obvious that the differences between the measurements and the simulations change spectrally, which might be caused by a non-homogeneous stratification of snow with different grain sizes or a moistening process taking place at the surface, such as melting snow. The latter one seems more likely because the albedo simulations were only done for dry snow conditions and the measurements are consistent with observations from Light et al. (2022) and Rosenberg et al. (2023).

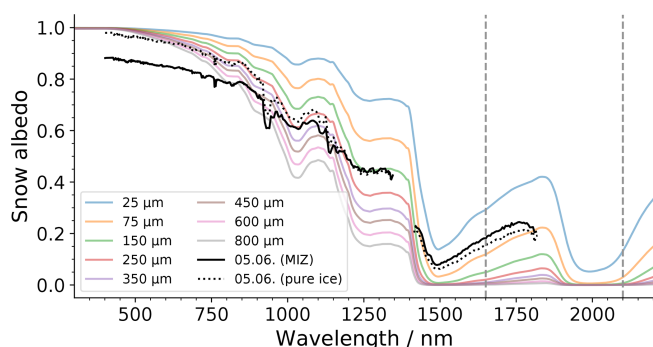


Figure 3. Measured (black) and simulated (colored) snow albedo. The measurements were taken during the ACLOUD flight on 5 June 2017 over pure sea ice (dotted line) and the marginal sea-ice zone (MIZ) (continuous line). The simulations cover grain sizes from 25 up to 800 μm and are based on Zege et al. (2011). The vertical dashed lines indicate the wavelengths (1650 and 2100 nm) which are used for the retrieval.

Figure 4a shows a 45 s sample of the spectral reflectivity from the combined measurements of AISA Hawk and SMART, which is shown for wavelengths 1650 and 2100 nm recorded for 45 s over Arctic sea ice during the *Polar 5* research flight on 24 March 2019. The spectral radiance along the 10 center across-track pixels (187–197) of the AISA Hawk samples is averaged to obtain upward-directed spectral radiance along the time of flight.

Look-up tables of R_λ were simulated for a liquid water cloud for different cloud properties by varying r_{eff} from 4 to 24 μm and LWP_{eff} from 3 to 390 g m^{-2} . The clouds are assumed to be homogeneous layers and follow the plane-parallel geometry of the radiative transfer model. The retrieval of r_{eff} from passive remote-sensing measurements is most sensitive to the cloud top layer, where absorption by cloud particles lowers the reflected radiance. By contrast, the scattering information in the measurements, which is linked to the retrieved LWP_{eff} , originates from the entire cloud. Therefore, retrieved cloud properties, especially LWP_{eff} , may depend on the vertical cloud structure. For this reason we use the index eff in LWP_{eff} to make it clear that this is an effective parameter based on passive remote-sensing measurements, which might be biased by the vertical cloud structure. The optical thickness, τ , is calculated by using LWP_{eff} and r_{eff} :

$$\tau = \frac{3}{2} \cdot \frac{\text{LWP}_{\text{eff}}}{\rho_w \cdot r_{\text{eff}}}, \quad (3)$$

with the density of water ρ_w . The assumption of homogeneous clouds and the neglect of 3D cloud structures follow the approach by Ruiz-Donoso et al. (2020) and are justified, especially when analyzing LWP_{eff} . As shown by Horváth et al. (2014), the 3D radiative effects are less pronounced in the retrieved LWP_{eff} compared to the optical thickness. Solar zenith angles were adjusted to the flight time and location.

A simulation was conducted for each AISA Hawk sample. The typical lengths of a sample were 3.6 min for ACLOUD and 2.1 min for AFLUX. For the flight section presented in Fig. 4a, the corresponding simulation is displayed as a retrieval grid in Fig. 5 assuming two different grain sizes. The reflectivities used here may still be affected by the variability of sea ice or snow albedo (Ehrlich et al., 2017).

The retrieval uses the reflectivity at 1650 nm wavelength and the reflectivity ratio of 2100 to 1650 nm wavelengths. This wavelength combination was chosen to minimize the dependence of sea ice and ocean surface albedo, similarly to Platnick (2001) and Ehrlich et al. (2017). The use of a ratio instead of a single wavelength reflectivity aims to increase the sensitivity to the cloud particle effective radius and to eliminate potential calibration biases (Werner et al., 2013; Ehrlich et al., 2017). To quantify the effect that different grain sizes of the surface snow layer had on the measurements of AFLUX and ACLOUD, the retrieval assumed two different snow grain sizes (150 and 600 μm). Figure 4b to d display the retrieved microphysical properties for grain sizes of 150 and 600 μm . The difference between both retrieval grids (see Fig. 5) indicates the uncertainties in the cloud retrieval due to the snow grain size. These uncertainties are largest for optically thin clouds with a low LWP and increase with droplet size. The set of exemplary measured data is located in a range where both retrieval grids match and the uncertainties due to the assumption of the snow grain size are lower. However, for the observed boundary-layer cloud, the difference between the retrieved r_{eff} is 1.2 % on average. It seems that, in the selected range of snow grain sizes, the assumption of the snow grain size has only a minor effect on the retrieval. Nevertheless, the closest agreement in Fig. 3 between simulations and measurements occurs for a snow grain size of 150 μm , which was finally selected for the albedo assumed in the retrieval. Since albedo measurements are not available for the AFLUX campaign, we use the same simulated albedo for this campaign as well.

The retrieval is limited by the assumption of pure liquid water clouds. As Arctic boundary-layer clouds are often characterized by a dominant liquid layer at the cloud top, the assumption of liquid clouds might be valid in many cases. Despite this assumption, the retrieval is applied to all boundary-layer clouds observed during the summer and spring campaigns independent of the cloud phase. Afterwards, to avoid ice-dominated cloud sections, we apply different filtering techniques to the retrieved data, which are described in the following section.

Filtering methods for liquid-dominated clouds

The retrieved microphysical liquid cloud properties over the Arctic sea ice and the ice-free ocean are often biased by ice crystals inside the clouds. To identify and neglect the biased measurements from our analysis, we apply three different filtering methods.

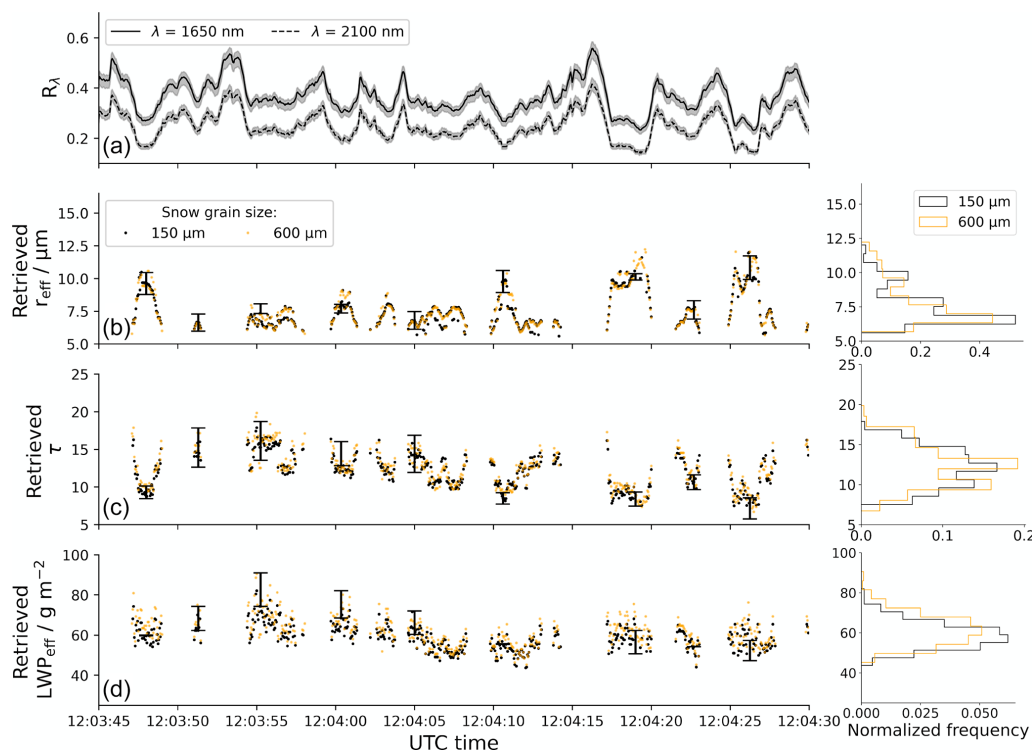


Figure 4. (a) Reflectivity, R_λ , calculated from AISA Hawk radiance along center pixels. The gray-shaded area indicates an AISA Hawk uncertainty of $\pm 6\%$. (b) Retrieved effective radius r_{eff} . (c) Retrieved optical thickness τ . (d) Retrieved effective liquid water path LWP_{eff} . The error bars for the retrieved parameters indicate an error propagation for an initial AISA Hawk uncertainty of $\pm 6\%$. All the observations were taken on 24 March 2019 during the AFLUX campaign.

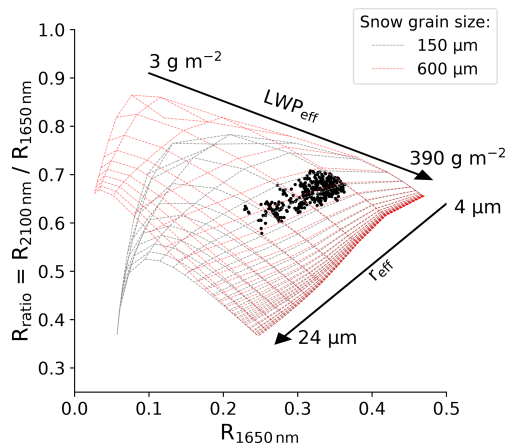


Figure 5. Retrieval grids combining the reflectivities at 1650 nm and the ratio of 2100 to 1650 nm for the measurement period shown in Fig. 4 from the AFLUX flight on 24 March 2019. The black dots indicate the reflectivities measured by AISA Hawk (see Eq. 1). The colors show the retrieval grid for snow grain sizes of 150 μm (gray) and 600 μm (red).

1. Equation (2) is applied to all the retrieval results. Only for $\text{PI} < 20$, which is an indicator of liquid clouds, are the retrieved values accepted for further analysis. This

method also removes cloud-free sections over sea ice because the detection of sea ice results in a high PI. Over the ocean, cloud-free sections are identified and removed when the LWP_{eff} is lower than 3 g m^{-2} .

2. We neglect all the reflectivity measurements, which are located outside the retrieval grid. These measurements are clearly biased and do not deliver plausible results.
3. We ignore AISA Hawk samples when less than 95 % of the reflectivity measurements are located inside the retrieval grid. This method is applied because ice crystals in clouds do not always move the reflectivity measurements outside the retrieval grid but partly shift them inside the retrieval grid. If 95 % of the measurements of an AISA Hawk sample are located inside the retrieval grid, it is very likely that the retrieved microphysical properties are not influenced by ice crystals. However, the disadvantage is a strong reduction of the dataset.

4 Retrieval uncertainties

Cloud properties are retrieved for the summer and spring campaigns, ALOUD and AFLUX, respectively. To identify the accuracy of the retrieval, we compare the retrieved cloud

properties with in situ observations using a case study. Furthermore, we use radar observations to identify the vertical cloud structure for which ice crystals potentially contaminate and bias the retrieved LWP_{eff} .

4.1 Comparing the retrieved cloud effective radius with in situ measurements

In situ measurements obtained during the AFLUX campaign for the flight on 24 March 2019 are used to evaluate the retrieved r_{eff} from AISA Hawk measurements. Two flight sections, one over the ice-free ocean and one over sea ice, both obtained shortly after or before the AISA Hawk measurements, are selected. The time series of radar reflectivity and flight altitude are shown in Fig. 6a together with the sea-ice concentration (dashed line) and the radar reflectivity. AISA Hawk sampled the first cloud top over an ice surface ($\sim 12:00$ UTC, $PI = 17.0$) just before *Polar 5* probed the cloud layer. The LWC profile in Fig. 6b, based on CAS measurements, shows the typical characteristics of clouds over sea ice, where clouds are driven by cloud top cooling and are located close to the surface, possibly touching the ground. The highest LWC is observed close to the surface.

For the second cloud ($\sim 14:20$ UTC, $PI = 14.6$), occurring over an ice-free water surface, *Polar 5* ascended through the cloud layer and conducted in situ measurements before AISA Hawk sampled the cloud top layer. Over the ice-free ocean (see Fig. 6c), the surface heat fluxes lead to a more convective cloud layer with a cloud base at 400 m and an adiabatic increase in LWC towards the cloud top. The in situ data are filtered for cloud LWC larger than 0.02 g m^{-3} to remove cloud droplets affected by mixing in the entrainment zone (Klingebiel et al., 2015).

The comparison between the retrieved r_{eff} and the directly measured r_{eff} by the in situ instruments is given for the first and second cloud cases in Fig. 6d and e, respectively. The cloud case over sea ice showed a rather complex multilayer cloud structure. As the retrieval by AISA Hawk is only sensitive to the cloud top, only in situ measurements of r_{eff} in the upper cloud layer around 2000 m altitude (the gray-shaded area in Fig. 6b) are used for the comparison. This layer is a pure liquid cloud with small droplet sizes and a median, measured with the in situ instruments, of $6.5 \mu\text{m}$. The lower cloud layers and the sea-ice surface do not significantly affect the AISA Hawk retrieval, which results in only a slightly larger r_{eff} with a median of $7.1 \mu\text{m}$.

While the majority of the effective radii in Fig. 6d occur below $10 \mu\text{m}$, the second case is characterized by larger droplets (Fig. 6e). Moreover, the in situ instruments detect particles in a size bin of up to $\sim 60 \mu\text{m}$, which indicates the presence of some ice particles. However, also in this case, the in situ and AISA Hawk measurements show close median values of 10.8 and $12.6 \mu\text{m}$, respectively. Considering that the AISA Hawk and in situ measurements were sampling the same cloud layer at different locations with completely

different measurement methods, the comparisons show in both cases (Fig. 6d and e) overlaps with close median values. This indicates that, for typically stratified mixed-phase clouds, the assumption of liquid clouds in the retrieval is valid. Filtering with $PI < 20$ (see Sect. 3a) ensures that only such liquid-dominated clouds are analyzed. Our presented retrieval method, thus, delivers reasonable results for the estimation of r_{eff} , even though the measurements took place under different surface conditions, i.e., ice-free ocean and sea ice, and in the presence of liquid-dominated mixed-phase clouds.

4.2 Comparing the retrieved optical thickness and liquid water path with in situ measurements

To evaluate the retrieved LWP_{eff} based on measurements of AISA Hawk, we integrate the LWC measured by the CAS in situ instrument between the cloud base and cloud top height of the sampled clouds. The vertical LWC profiles of the CAS are presented together with the IWC from the CIP instrument in Fig. 6b and c for the first and second cloud sections, respectively. The profiles capture the whole vertical descent and ascent through the clouds, limited only by the minimum flight altitude of 60 m.

In contrast to the retrieval of r_{eff} , the LWP_{eff} retrieved from AISA Hawk is an integral value over the entire altitude below the aircraft. The in situ calculated LWP over sea ice (Fig. 6b) is 21 g m^{-2} . For the cloud over the ice-free ocean (Fig. 6c), a value of 101 g m^{-2} is derived. The in situ LWP for the first section might underestimate the real cloud because parts of the cloud below the flight altitude were not sampled.

The retrieved LWP_{eff} averaged over the AISA Hawk samples are 62 and 119 g m^{-2} (21 and 101 g m^{-2} were measured by the in situ instruments) for the first and second cloud cases, respectively. For the cloud over sea ice, LWP_{eff} is overestimated by a factor of 3 by AISA Hawk. Both cases showed significant IWP, which is quantified by the in situ measurements. The retrieval by AISA Hawk assumes the entire cloud to be liquid. Therefore, IWP is to some extent included in the retrieved LWP_{eff} , which will overestimate the in situ LWP. Additionally, a bias in the retrieved r_{eff} due to the presence of ice particles will lead to an overestimation of LWP_{eff} by the retrieval. This is a known problem of the retrieval method when assuming homogeneous liquid vertical profiles and applying it to mixed-phase clouds (Coopman et al., 2019; Ruiz-Donoso et al., 2020). Considering the IWC profiles in Fig. 6b and c, it is obvious that ice particles were present inside the clouds and lead to precipitation (snow) in the lower cloud layers. Only the top layer (around 2000 m altitude) for the first cloud consisted of pure liquid droplets, which were sampled by the AISA Hawk instrument. All in all, the differences between the measured and retrieved liquid water paths seem to be influenced by the distributions of ice particles and liquid water inside the cloud.

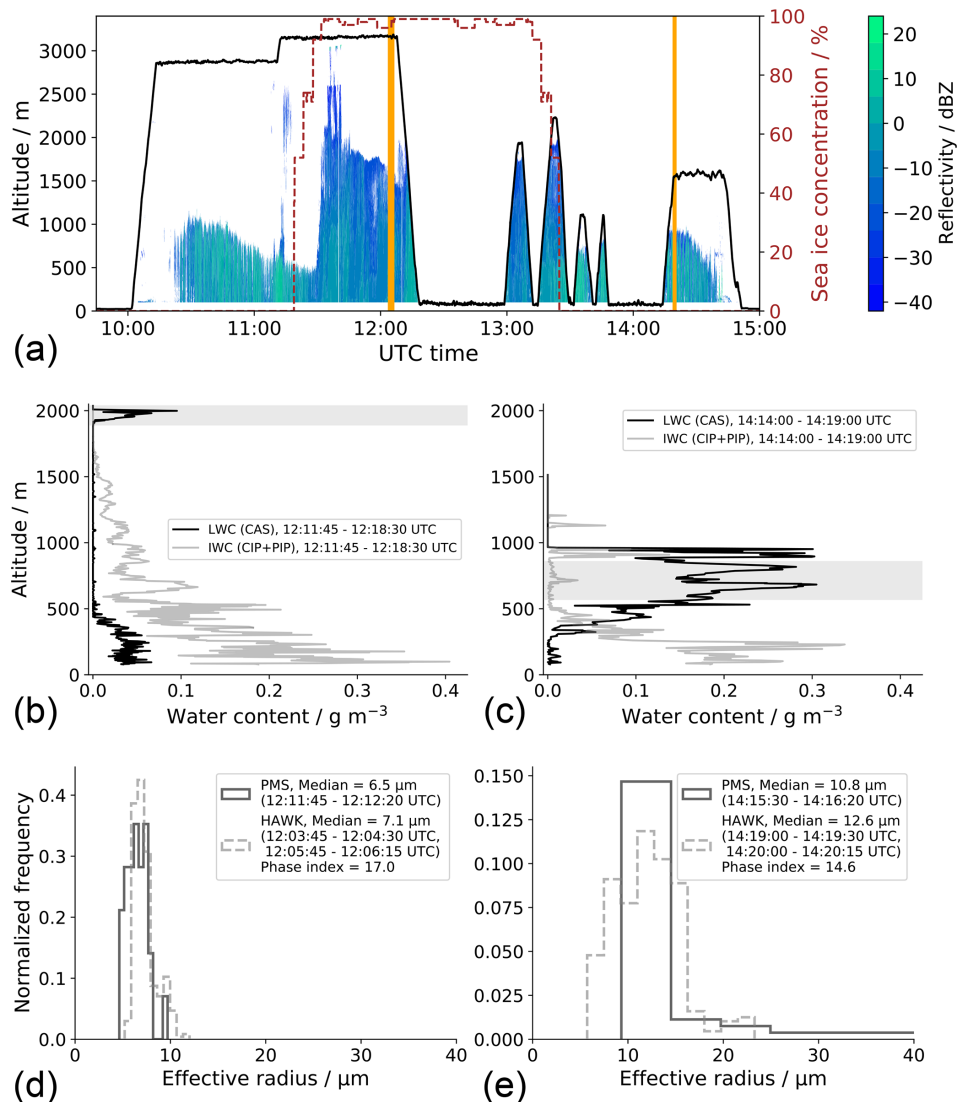


Figure 6. (a) Sea-ice concentration based on AMSR-E observations (dashed line) and the altitude profile (black) of the *Polar 5* flight on 24 March 2019 during AFLUX. The vertical lines (orange) indicate the AISA Hawk measurements, which are shown in panels (d) and (e). The radar reflectivity of the sampled clouds is indicated by the color bar. (b) Measured LWC and IWC profiles from the CAS, CIP and PIP instruments during the descent around 12:10 UTC. (c) Same as panel (b) but for the ascent through the cloud layer around 14:15 UTC. The gray-shaded areas mark the sections which were considered for the in situ measurements of r_{eff} . (d) Histogram of the retrieved effective radius for different flight sections, both retrieved over sea ice and compared with in situ measurements. (e) Same as panel (d) but retrieved and measured over the ice-free ocean. The in situ measurements in panels (d) and (e) were taken during vertical profiles of *Polar 5* through the cloud layers.

To constrain the impact of ice particles on the retrieval biases, the in situ measurements are converted to extinction profiles of liquid and ice particles following the theory of Eq. (3). The profiles are integrated into the in situ cloud optical thicknesses for total, liquid and ice particles. If the extinction by ice particles is low and the extinction by liquid droplets matches the retrieved τ , the observed bias of LWP_{eff} is mostly due to the assumption of homogeneous clouds. This is the case for the second cloud section, where cloud optical thicknesses of 16.1 (retrieved), 16.35 (in situ total), 15.97 (in

situ liquid) and 0.37 (in situ ice) were derived. For the first section, the comparison does fail – 13.2 (retrieved), 2.6 (in situ total), 1.95 (in situ liquid) and 0.65 (in situ ice) – due to the mismatch of the cloud location. This is obvious in the radar reflectivity (see Fig. 6a), which significantly increases after the remote-sensing measurement and while starting the in situ profile. The high radar reflectivity agrees with the high amount of IWC measured in situ (Fig. 6b). During the AISA Hawk measurements, the radar reflectivity was still lower, indicating a more liquid-dominated cloud. Unfortunately, this

makes a comparison of the LWP_{eff} and optical thickness impossible for this section. However, the agreement in retrieved and in situ r_{eff} at least indicates that the liquid cloud top layer did not significantly change.

4.3 Statistical evaluation of the retrieval using cloud radar observations

As indicated by the case study, the location of ice particles within the cloud column may bias the retrieved LWP_{eff} . In Arctic mixed-phase clouds, the vertical structure and the number of ice particles may change on small scales, which is often linked to updrafts and downdrafts of the cloud (Ruiz-Donoso et al., 2020). A way to quantify how often the retrieval is affected by the presence of ice crystals is to look at the position of the measurements regarding the retrieval grid. For example, in Fig. 5, all the measurements (black dots) are within the retrieval grid, which indicates plausible results even though there are uncertainties for the LWP_{eff} . However, if the observed cloud layer, in particular the cloud top, is dominated by ice particles, then the measurements are affected and might move outside the retrieval grid, as is shown in Fig. 7b in Ruiz-Donoso et al. (2020). Therefore, the position of the measurements relative to the retrieval grid is an indicator of how reliable the retrieved results are.

Nevertheless, unlike the PI, this indicator does not provide any information on whether a boundary-layer cloud is dominated by liquid water or ice particles. To make that clearer, Fig. 7 shows for both campaigns the distribution of the PI depending on the positions of the measurements inside the retrieval grid. While for the ALOUD campaign (Fig. 7a) the distributions look similar, they show some differences for the AFLUX campaign (Fig. 7b). As AFLUX was characterized by colder temperatures favoring the presence of mixed-phase clouds, measurements are located more often outside the retrieval grid when the PI is higher. Nevertheless, it becomes clear that the position of the measurements relative to the retrieval grid cannot be used as an indicator of the number of ice particles inside a boundary-layer cloud because the PI is not directly linked to the position of the measurements inside and outside the retrieval grid.

To identify how reliable the retrieval results are, we analyze how often the measurements are located inside the retrieval grid for both campaigns. The results are presented in Table 1. For AFLUX, 19 % and 13 % of the measurements lie inside the retrieval grid over a sea-ice-free surface and over a sea-ice surface. During the ALOUD campaign, 22 % of the measurements were covered by the retrieval grid over a water surface and up to 42 % over an ice surface. These numbers indicate that fewer cloud ice particles were present during ALOUD than during AFLUX, which is related to the lower atmospheric temperatures (see Fig. 2) because ALOUD was conducted later in the year.

To estimate the ice concentration that is responsible for a mismatch between the measurements and the retrieval grid,

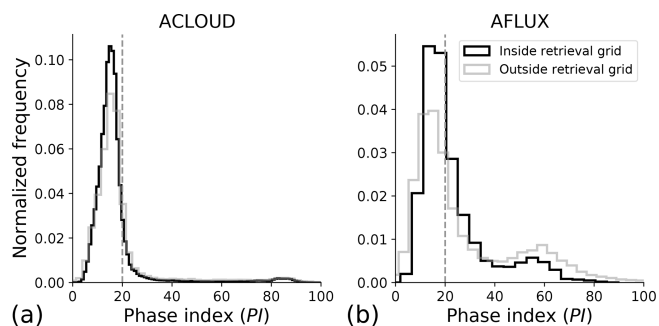


Figure 7. Distribution of the PI for the ALOUD (a) and AFLUX (b) campaigns, depending on the locations of the AISA Hawk measurements related to the retrieval grid. The vertical dashed lines indicate the threshold that is used to discriminate between liquid and mixed-phase clouds.

we use the MiRAC cloud radar measurements from both campaigns. The cloud radar is sensitive to ice particles and measures the portion of ice inside the clouds, which is shown by the detected radar reflectivity. Figure 8 shows the distribution of the radar reflectivity for measurements inside and outside the retrieval grid. To avoid retrieval cases with measurements simultaneously inside and outside the retrieval grid, we only consider AISA Hawk samples with more than 95 % of the measurements inside the retrieval grid, as is explained in Sect. 3. Unfortunately, this reduces the amount of data to 7 % for ALOUD and 2 % for AFLUX.

Figure 8a shows the highest contributions of ice particles below 1500 m of between -20 and -10 dBZ. These signals are related to snow, which shows values of up to 15 dBZ below 1500 m. Between 1500 and 3500 m, the maximum radar reflectivity increases to 0 dBZ. In Fig. 8b, the precipitation below 1500 m is visible as well. Above 1500 m the radar reflectivities show values of up to 5 dBZ, which is higher than in Fig. 8a.

To emphasize the difference between Fig. 8a and b, we show in Fig. 8c the profiles of the CFAD plots from Fig. 8a and b and only consider the maximum dBZ values with densities larger than 0.015 %. Here it is obvious that, when the AISA Hawk measurements end up outside the retrieval grid and the retrieval fails, the radar reflectivities are higher in the cloud top layers (see the dashed line between 1500 and 3500 m). A higher radar reflectivity indicates more ice particles inside the clouds, which affects the retrieval method. It can be concluded that the retrieval fails if the radar reflectivity in the cloud top layer is larger than -5 dBZ.

The same analysis is done for the spring campaign, AFLUX, and the results are presented in Fig. 8d to f. Here, it is noticeable that the cloud top is lower than during the summer campaign, ALOUD. This agrees with Mioche et al. (2015), who reported lower cloud tops during the winter than during the summer months in the vicinity of Svalbard. For the spring campaign, the retrieval failed more often (see Table 1),

Table 1. Number of recorded AISA Hawk data from the ACloud and AFLUX campaigns. One data point represents one pixel value along the center pixel line of an AISA Hawk sample.

| | ACloud | AFLUX |
|--|-------------------|------------------|
| All data | 1 079 508 (100 %) | 907 091 (100 %) |
| Data over the sea-ice surface | 717 857 (66.5 %) | 413 982 (45.6 %) |
| Data over the sea-ice-free surface | 361 651 (33.5 %) | 493 109 (54.4 %) |
| Data over the sea-ice surface inside the retrieval grid | 448 089 (41.5 %) | 120 427 (13.3 %) |
| Data over the sea-ice-free surface inside the retrieval grid | 234 873 (21.8 %) | 170 796 (18.8 %) |

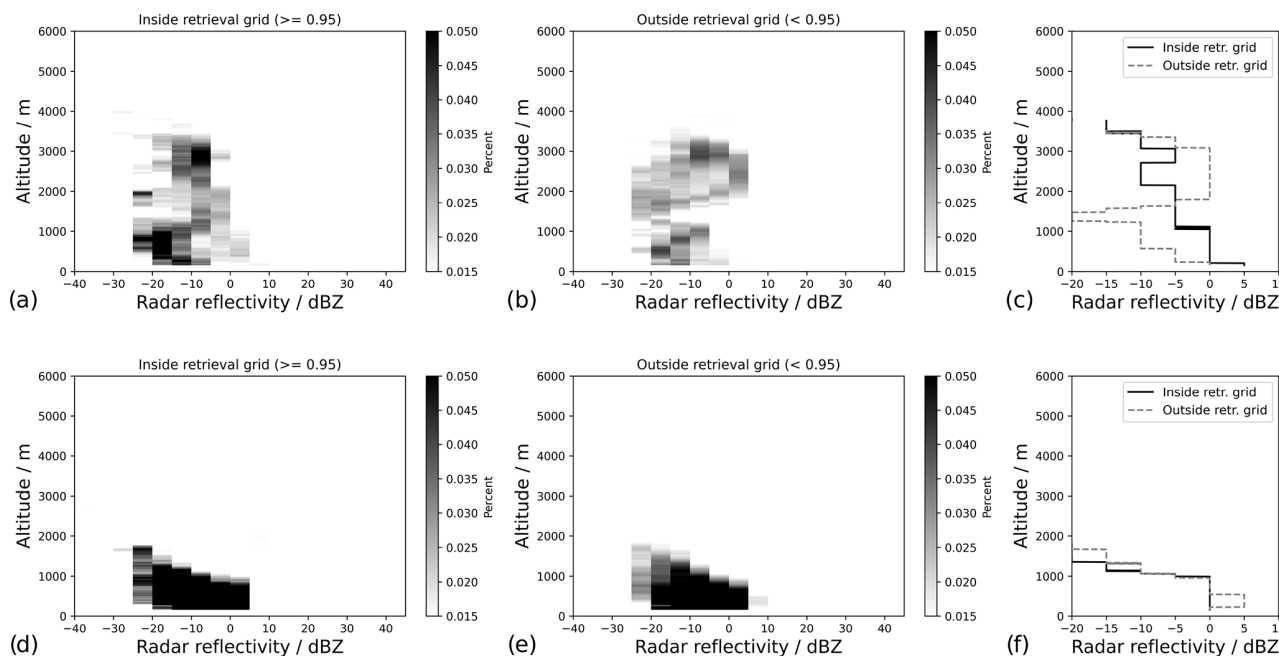


Figure 8. (a) Contoured frequency by altitude diagram (CFAD) for the ACloud campaign when 95 % of the measurements of each AISA Hawk sample were within the retrieval grid. (b) CFAD of the same measurements, but here less than 95 % were within the retrieval grid. (c) Profiles of the CFAD plots in panels (a) and (b) considering the maximum dBZ values with densities > 0.015 %. Panels (d) to (f) show the same but for the AFLUX campaign.

which is related to a higher portion of ice particles inside the sampled clouds (see Fig. 7b). Therefore, the results in Fig. 8d to f are not as obvious as for the summer campaign (Fig. 8a to c).

5 Comparison of retrieved cloud properties over Arctic sea ice and the ice-free ocean

The retrieval results of both campaigns are compared to each other to identify the differences in the liquid water cloud properties over the ice-free ocean and Arctic sea ice. To make sure that we only consider liquid water clouds, we present for the retrieved parameters clouds with $PI < 20$, and we neglect AISA Hawk measurements located outside the retrieval grid. These are the filtering methods 1 and 2 described in Sect. 3. The results are shown as distribution plots in Fig. 9 and show the PI , r_{eff} , τ and LWP_{eff} .

The third filtering method (samples with less than 95 % of the reflectivity measurements located inside the retrieval grid are ignored) was also applied, but, as mentioned before, it reduces the dataset to 7 % for ACloud and 2 % for AFLUX. Nevertheless, we have high confidence in the retrieval results shown in Fig. 9 because the differences in the results considering the third filtering method are very minor. This is shown in Table 2 by the median values of the distribution plots for both filtering methods. Moreover, in the early summer, the liquid-phase clouds have larger median values of $r_{\text{eff}} = 9.5 \mu\text{m}$, $\tau = 11.8$ and $LWP_{\text{eff}} = 72.3 \text{ g m}^{-2}$ in comparison to spring conditions ($8.7 \mu\text{m}$, 8.3 and 51.8 g m^{-2} , respectively). That the values of the microphysical cloud properties are larger in summer is also valid for the observations over water and over the sea-ice surface.

The distribution plots of the PI (Fig. 9a) show for the majority of ACloud and AFLUX measurements $PI < 20$

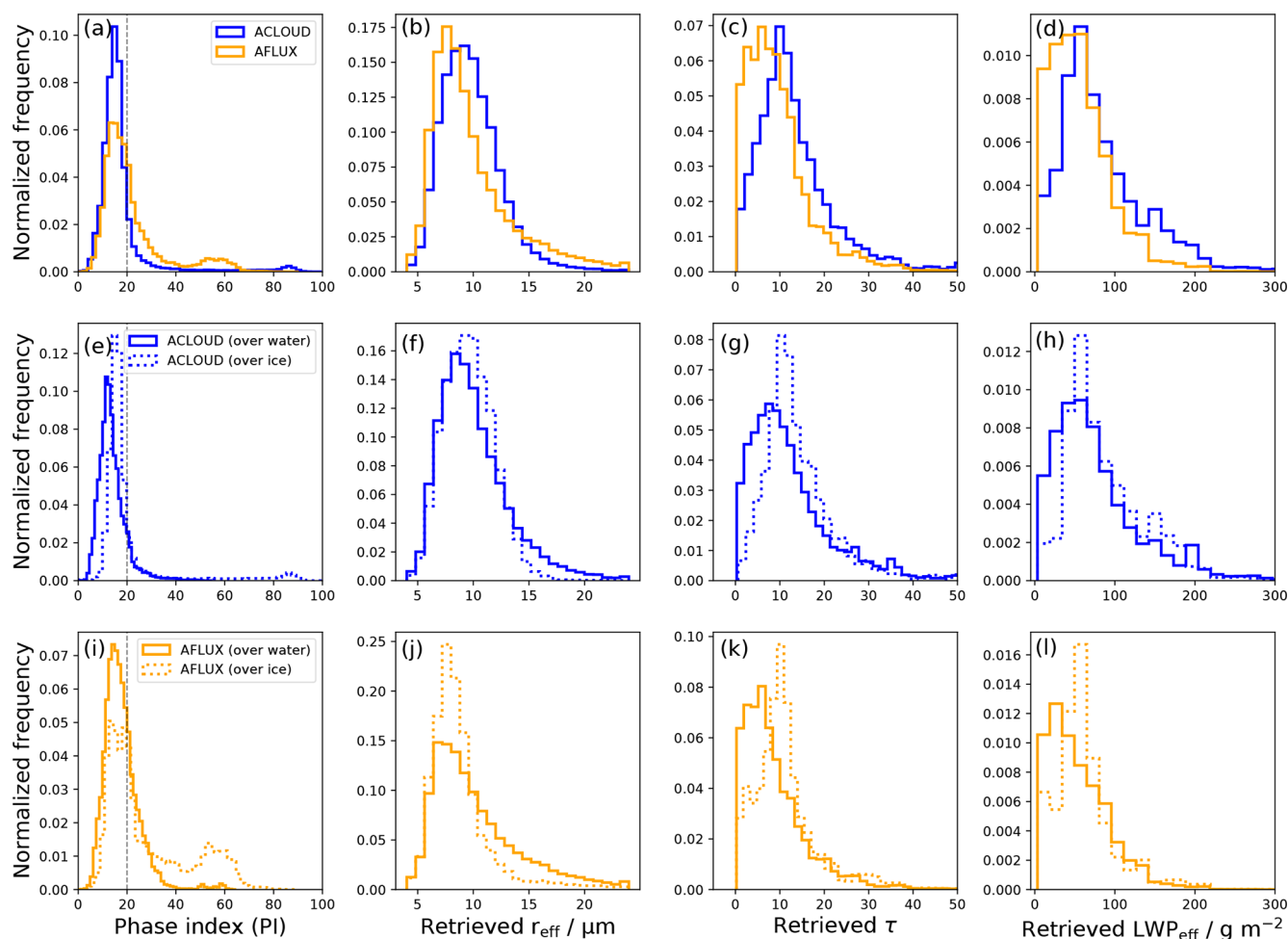


Figure 9. Comparison between the early summer, ACloud, and spring, AFLUX, campaigns. Panels (a)–(d) show the differences in the phase index and the retrieved parameters r_{eff} , τ and LWP_{eff} over ice-free water and sea ice. Panels (e)–(h) and panels (i)–(l) show the same parameters but exclusively for the ACloud and AFLUX campaigns, respectively. Here, the data are separated into measurements over ice-free water (solid lines) and sea ice (dotted lines).

(dashed vertical line), which means that the observed cloud tops were dominated by liquid water droplets. However, observations with $\text{PI} > 20$, which represents the occurrence of ice particles or surface ice measured through optically thin clouds, are common to both campaigns. Two peaks are noticeable around PIs of 60 and 85 (see Fig. 9a) and indicate higher in-cloud ice concentrations. Figure 9e and i support these peaks being detected over ice. A closer look at the nadir camera pictures from these flight segments revealed that, for the peak detected during AFLUX, a haze layer was located over the ice, while for ACloud barely any clouds were visible, so that the PI represents in this case the pure ice surface.

As discussed before, the retrieval method is suited to liquid water clouds and fails when ice particles are present. That is why the clouds are optically thicker in Fig. 9g and k over a sea-ice surface, because optically thin clouds, where the ice on the surface increases the PI, are not considered.

The r_{eff} shows larger values over the open ocean than over sea ice for both campaigns (see Fig. 9f and j). This is plausible because the moister and warmer air over the open ocean leads to more convection and, therefore, higher cloud tops with larger cloud droplets. Larger cloud droplets over ice-free water consequently lead to a smaller optical thickness, τ , which is shown in Fig. 9g and k by a shift in the over-water modes towards a smaller τ .

Focusing on the ice-free ocean, the LWP_{eff} peaks around 20 g m^{-2} during AFLUX, while it peaks around 50 g m^{-2} during ACloud. This difference might be related to the seasons. ACloud took place roughly 2 months later in the year with higher temperatures, and hence the clouds might have evolved more and produced more liquid water. Despite the different seasons, the LWP_{eff} over sea ice is similar for both campaigns, which indicates that, over sea ice, the changes might not be as significant as they are over water.

Table 2. Median values of the retrieved cloud properties and the slope phase index considering data inside the retrieval grid from all the samples (see Fig. 9) compared to median values considering only samples with 95 % of the measurements located inside the retrieval grid.

| | | All sampled data inside the grid | | Samples with 95 % of the data inside the grid | | Difference | |
|---------------|---|-------------------------------------|-------|--|-------|------------|-------|
| | | ACLOUD | AFLUX | ACLOUD | AFLUX | ACLOUD | AFLUX |
| All | PI | 15.1 | 17.9 | 13.4 | 13.5 | 1.7 | 4.4 |
| | r_{eff} (μm) | 9.5 | 8.7 | 9.3 | 8.5 | 0.2 | 0.2 |
| | τ | 11.8 | 8.3 | 11.5 | 8.4 | 0.3 | -0.1 |
| | LWP_{eff} (g m^{-2}) | 72.3 | 51.8 | 69.2 | 49.1 | 3.1 | 2.7 |
| Over water | PI | 12.8 | 16.5 | 12.4 | 14.4 | 0.4 | 2.1 |
| | r_{eff} (μm) | 9.4 | 9.1 | 9.3 | 11.8 | 0.1 | -2.7 |
| | τ | 10.4 | 7.1 | 10.1 | 6.1 | 0.3 | 1.0 |
| | LWP_{eff} (g m^{-2}) | 65.8 | 48.0 | 62.6 | 51.8 | 3.2 | -3.8 |
| Over ice | PI | 16.1 | 20.8 | 15.3 | 13.0 | 0.8 | 7.8 |
| | r_{eff} (μm) | 9.5 | 8.1 | 9.5 | 8.0 | 0.0 | 0.1 |
| | τ | 12.5 | 10.2 | 13.1 | 9.3 | -0.6 | 0.9 |
| | LWP_{eff} (g m^{-2}) | 77.4 | 56.8 | 85.1 | 48.3 | -7.7 | 8.5 |

6 Conclusions

Airborne solar spectral radiance measurements from cloud tops are used to retrieve cloud microphysical properties of Arctic liquid-phase clouds during the summer campaign ACLOUD in May and June 2017 and the spring campaign AFLUX in March and April 2019 in the vicinity of Svalbard.

The retrieval method presented in this study is developed for liquid water clouds and, therefore, involves three different filtering techniques to avoid cloud top sections, which are dominated by ice crystals. That the retrieval is applicable for Arctic mixed-phase clouds, which are often covered by a super-cooled liquid cloud top layer, is shown by a comparison of the retrieved cloud top r_{eff} with in situ measurements. In a case study, the retrieved r_{eff} with median values of 7.1 and 12.6 μm showed good agreement with in situ measurements with median values of 6.5 and 10.8 μm , respectively, even considering that the measurements were performed successively.

However, the retrieved LWP_{eff} is overestimated, which is a known issue for this kind of retrieval method and is related to ice particles inside the clouds because the retrieval is suited for pure liquid water clouds.

To identify how much cloud ice the retrieval can tolerate and how the ice needs to be distributed vertically to affect the retrieval results, we compare the retrieval results with radar measurements. The comparison leads to the conclusion that the retrieval method is reliable when the radar reflectivity of the cloud top layer is smaller than -5 dBZ.

Considering these limitations, we applied the retrieval method to a dataset of airborne measurements of cloud top spectral solar radiances of Arctic boundary-layer clouds to characterize the differences between microphysical properties of clouds observed over the ice-free ocean and Arctic

sea ice in spring and early summer in the vicinity of Svalbard. We identified that, in early summer, the liquid-phase clouds have larger median values of $r_{\text{eff}} = 9.5 \mu\text{m}$, $\tau = 11.8$ and $\text{LWP}_{\text{eff}} = 72.3 \text{ g m}^{-2}$ in comparison to spring conditions (8.7 μm , 8.3 and 51.8 g m^{-2} , respectively). These differences might be related to the temperature differences between the summer and spring campaigns. Independent of the season, the results show larger cloud droplets over the ice-free ocean compared to the Arctic sea ice. This seems to be caused by the temperature and humidity differences in the surfaces and related convection processes. Because the sizes of the cloud droplets are larger over the ice-free ocean, τ and LWP_{eff} are slightly reduced.

In summary, the presented and comprehensive dataset shows the microphysical differences in liquid-phase clouds over Arctic sea ice and the ice-free ocean for summer and spring conditions. The data are publicly available (Klingebiel et al., 2023a, b) and can be used for studies to constrain models which investigate the effects of Arctic boundary-layer clouds on the radiation budget.

Data availability. The comprehensive datasets presented here on microphysical properties of Arctic liquid-phase clouds have been published in <https://doi.org/10.1594/PANGAEA.960907> (Klingebiel et al., 2023a) and <https://doi.org/10.1594/PANGAEA.960906> (Klingebiel et al., 2023b). The SMART data used in this study have been published in <https://doi.org/10.1594/PANGAEA.899177> (Jäkel et al., 2019a). All AISA Hawk spectral radiance measurements from the ACLOUD and AFLUX campaigns have been published in <https://doi.org/10.1594/PANGAEA.902150> (Ruiz-Donoso et al., 2019) and <https://doi.org/10.1594/PANGAEA.930932> (Schäfer et al., 2021). The measurements from the in situ instruments have

been published in <https://doi.org/10.1594/PANGAEA.940564> (Moser and Voigt, 2022). The flight track data are from <https://doi.org/10.1594/PANGAEA.888173> (Ehrlich et al., 2018) and <https://doi.org/10.1594/PANGAEA.902876> (Lüpkes et al., 2019).

Author contributions. MK is the primary author of the paper. AE, ERD, EJ, MS, KW, MMe and MMo, CV and MW carried out the airborne experimental work. Simulations with libRadtran were performed by ERD, KW and MK. MK and MMo compared the retrieval results with in situ measurements. NR, IS and MK evaluated the accuracy of the retrieval results with radar observations. All the authors contributed to the interpretation of the results and wrote the paper.

Competing interests. The contact author has declared that none of the authors has any competing interests.

Disclaimer. Publisher's note: Copernicus Publications remains neutral with regard to jurisdictional claims made in the text, published maps, institutional affiliations, or any other geographical representation in this paper. While Copernicus Publications makes every effort to include appropriate place names, the final responsibility lies with the authors.

Acknowledgements. Scientific support was given by Anna E. Luebke. We give special thanks to the whole research team, including the engineers and pilots from the ACLOUD and AFLUX campaigns. We would also like to thank two anonymous reviewers, who had very helpful comments regarding this publication. We gratefully acknowledge the funding by the Deutsche Forschungsgemeinschaft (DFG, German Research Foundation) – grant no. 268020496 – TRR 172, within the Transregional Collaborative Research Center ArctiC Amplification: Climate Relevant Atmospheric and SurfaCe Processes and Feedback Mechanisms (AC)³.

Financial support. This research has been supported by the Deutsche Forschungsgemeinschaft (grant no. 268020496 – TRR 172, grant no. 428312742 – TRR 301 and Priority Program SPP PROM VO 1504/5-1) and financed by the Open Access Publishing Fund of Leipzig University supported by the German Research Foundation within the Open Access Publication Funding program.

Review statement. This paper was edited by Duncan Watson-Parris and reviewed by two anonymous referees.

References

- Baumgardner, D., Jonsson, H., Dawson, W., O'Connor, D., and Newton, R.: The cloud, aerosol and precipitation spectrometer: a new instrument for cloud investigations, *Atmos. Res.*, 59–60, 251–264, [https://doi.org/10.1016/s0169-8095\(01\)00119-3](https://doi.org/10.1016/s0169-8095(01)00119-3), 2001.
- Baumgardner, D., Abel, S. J., Axisa, D., Cotton, R., Crosier, J., Field, P., Gurganus, C., Heymsfield, A., Korolev, A., Krämer, M., Lawson, P., McFarquhar, G., Ulanowski, Z., and Um, J.: Cloud Ice Properties: In Situ Measurement Challenges, *Meteor. Mon.*, 58, 9.1–9.23, <https://doi.org/10.1175/amsmonographs-d-16-0011.1>, 2017.
- Bierwirth, E., Ehrlich, A., Wendisch, M., Gayet, J.-F., Gourbeyre, C., Dupuy, R., Herber, A., Neuber, R., and Lampert, A.: Optical thickness and effective radius of Arctic boundary-layer clouds retrieved from airborne nadir and imaging spectrometry, *Atmos. Meas. Tech.*, 6, 1189–1200, <https://doi.org/10.5194/amt-6-1189-2013>, 2013.
- Coopman, Q., Hoose, C., and Stengel, M.: Detection of Mixed-Phase Convective Clouds by a Binary Phase Information From the Passive Geostationary Instrument SEVIRI, *J. Geophys. Res.-Atmos.*, 124, 5045–5057, <https://doi.org/10.1029/2018JD029772>, 2019.
- Ehrlich, A., Bierwirth, E., Wendisch, M., Gayet, J.-F., Mioche, G., Lampert, A., and Heintzenberg, J.: Cloud phase identification of Arctic boundary-layer clouds from airborne spectral reflection measurements: test of three approaches, *Atmos. Chem. Phys.*, 8, 7493–7505, <https://doi.org/10.5194/acp-8-7493-2008>, 2008.
- Ehrlich, A., Bierwirth, E., Istomina, L., and Wendisch, M.: Combined retrieval of Arctic liquid water cloud and surface snow properties using airborne spectral solar remote sensing, *Atmos. Meas. Tech.*, 10, 3215–3230, <https://doi.org/10.5194/amt-10-3215-2017>, 2017.
- Ehrlich, A., Wendisch, M., Lüpkes, C., Crewell, S., and Mech, M.: Master tracks in different resolutions during POLAR 5 campaign ACLOUD₂₀₁₇, PANGAEA [data set], <https://doi.org/10.1594/PANGAEA.888173>, 2018.
- Ehrlich, A., Wendisch, M., Lüpkes, C., Buschmann, M., Bozem, H., Chechin, D., Clemen, H.-C., Dupuy, R., Eppers, O., Hartmann, J., Herber, A., Jäkel, E., Järvinen, E., Jourdan, O., Kästner, U., Kliesch, L.-L., Köllner, F., Mech, M., Mertes, S., Neuber, R., Ruiz-Donoso, E., Schnaiter, M., Schneider, J., Stapf, J., and Zanatta, M.: A comprehensive in situ and remote sensing data set from the Arctic CLOUD Observations Using airborne measurements during polar Day (ACLOUD) campaign, *Earth Syst. Sci. Data*, 11, 1853–1881, <https://doi.org/10.5194/essd-11-1853-2019>, 2019.
- Ehrlich, A., Zöger, M., Giez, A., Nenakhov, V., Mallaun, C., Maser, R., Rösenthaler, T., Luebke, A. E., Wolf, K., Stevens, B., and Wendisch, M.: A new airborne broadband radiometer system and an efficient method to correct dynamic thermal offsets, *Atmos. Meas. Tech.*, 16, 1563–1581, <https://doi.org/10.5194/amt-16-1563-2023>, 2023.
- Emde, C., Buras-Schnell, R., Kylling, A., Mayer, B., Gasteiger, J., Hamann, U., Kylling, J., Richter, B., Pause, C., Dowling, T., and Bugliaro, L.: The libRadtran software package for radiative transfer calculations (version 2.0.1), *Geosci. Model Dev.*, 9, 1647–1672, <https://doi.org/10.5194/gmd-9-1647-2016>, 2016.

- Faber, S., French, J. R., and Jackson, R.: Laboratory and in-flight evaluation of measurement uncertainties from a commercial Cloud Droplet Probe (CDP), *Atmos. Meas. Tech.*, 11, 3645–3659, <https://doi.org/10.5194/amt-11-3645-2018>, 2018.
- Fricke, C., Ehrlich, A., Jäkel, E., Bohn, B., Wirth, M., and Wendisch, M.: Influence of local surface albedo variability and ice crystal shape on passive remote sensing of thin cirrus, *Atmos. Chem. Phys.*, 14, 1943–1958, <https://doi.org/10.5194/acp-14-1943-2014>, 2014.
- Gurganus, C. and Lawson, P.: Laboratory and Flight Tests of 2D Imaging Probes: Toward a Better Understanding of Instrument Performance and the Impact on Archived Data, *J. Atmos. Ocean. Tech.*, 35, 1533–1553, <https://doi.org/10.1175/jtech-d-17-0202.1>, 2018.
- Heymsfield, A. J., Schmitt, C., Bansemer, A., and Twohy, C. H.: Improved Representation of Ice Particle Masses Based on Observations in Natural Clouds, *J. Atmos. Sci.*, 67, 3303–3318, <https://doi.org/10.1175/2010jas3507.1>, 2010.
- Hogan, R. J., Tian, L., Brown, P. R. A., Westbrook, C. D., Heymsfield, A. J., and Eastment, J. D.: Radar Scattering from Ice Aggregates Using the Horizontally Aligned Oblate Spheroid Approximation, *J. Appl. Meteorol. Clim.*, 51, 655–671, <https://doi.org/10.1175/jamc-d-11-074.1>, 2012.
- Horváth, A., Seethala, C., and Deneke, H.: View angle dependence of MODIS liquid water path retrievals in warm oceanic clouds, *J. Geophys. Res.-Atmos.*, 119, 8304–8328, <https://doi.org/10.1002/2013JD021355>, 2014.
- Jäkel, E., Ehrlich, A., Schäfer, M., and Wendisch, M.: Aircraft measurements of spectral solar up- and downward irradiances in the Arctic during the ALOUD campaign 2017, Universität Leipzig, PANGAEA [data set], <https://doi.org/10.1594/PANGAEA.899177>, 2019a.
- Jäkel, E., Stapf, J., Wendisch, M., Nicolaus, M., Dorn, W., and Rinke, A.: Validation of the sea ice surface albedo scheme of the regional climate model HIRHAM–NAOSIM using aircraft measurements during the ALOUD/PASCAL campaigns, *The Cryosphere*, 13, 1695–1708, <https://doi.org/10.5194/tc-13-1695-2019>, 2019b.
- Jäkel, E., Carlsen, T., Ehrlich, A., Wendisch, M., Schäfer, M., Rosenburg, S., Nakoudi, K., Zanatta, M., Birnbaum, G., Helm, V., Herber, A., Istomina, L., Mei, L., and Rohde, A.: Measurements and Modeling of Optical-Equivalent Snow Grain Sizes under Arctic Low-Sun Conditions, *Remote Sens.*, 13, 4904, <https://doi.org/10.3390/rs13234904>, 2021.
- Kleine, J., Voigt, C., Sauer, D., Schlager, H., Scheibe, M., Jurkat-Witschas, T., Kaufmann, S., Kärcher, B., and Anderson, B. E.: In situ observations of ice particle losses in a young persistent contrail, *Geophysical Research Lett.*, 45, 13553–13561, <https://doi.org/10.1029/2018GL079390>, 2018.
- Kliesch, L.-L. and Mech, M.: Airborne radar reflectivity and brightness temperature measurements with POLAR 5 during ALOUD in May and June 2017, PANGAEA [data set], <https://doi.org/10.1594/PANGAEA.899565>, 2019.
- Klingebiel, M., de Lozar, A., Molleker, S., Weigel, R., Roth, A., Schmidt, L., Meyer, J., Ehrlich, A., Neuber, R., Wendisch, M., and Borrmann, S.: Arctic low-level boundary layer clouds: in situ measurements and simulations of mono- and bimodal supercooled droplet size distributions at the top layer of liquid phase clouds, *Atmos. Chem. Phys.*, 15, 617–631, <https://doi.org/10.5194/acp-15-617-2015>, 2015.
- Klingebiel, M., Ehrlich, A., Jäkel, E., Schäfer, M., Ruiz-Donoso, E., Wolf, K., and Wendisch, M.: Properties of liquid-dominated clouds over the ice-free and sea-ice-covered Arctic Ocean during ALOUD, PANGAEA [data set], <https://doi.org/10.1594/PANGAEA.960907>, 2023a.
- Klingebiel, M., Ehrlich, A., Jäkel, E., Schäfer, M., Ruiz-Donoso, E., Wolf, K., and Wendisch, M.: Properties of liquid-dominated clouds over the ice-free and sea-ice-covered Arctic Ocean during AFLUX, PANGAEA [data set], <https://doi.org/10.1594/PANGAEA.960906>, 2023b.
- Korolev, A., McFarquhar, G., Field, P. R., Franklin, C., Lawson, P., Wang, Z., Williams, E., Abel, S. J., Axisa, D., Borrmann, S., Crosier, J., Fugal, J., Krämer, M., Lohmann, U., Schlenker, O., Schnaiter, M., and Wendisch, M.: Mixed-Phase Clouds: Progress and Challenges, *Meteor. Mon.*, 58, 5.1–5.50, <https://doi.org/10.1175/amsmonographs-d-17-0001.1>, 2017.
- Light, B., Smith, M. M., Perovich, D. K., Webster, M. A., Holland, M. M., Linhardt, F., Raphael, I. A., Clemens-Sewall, D., Macfarlane, A. R., Anhaus, P., and Bailey, D. A.: Arctic sea ice albedo: Spectral composition, spatial heterogeneity, and temporal evolution observed during the MOSAiC drift, *Elem. Sci. Anth.*, 10, 000103, <https://doi.org/10.1525/elementa.2021.000103>, 2022.
- Liu, Y., Ackerman, S. A., Maddux, B. C., Key, J. R., and Frey, R. A.: Errors in Cloud Detection over the Arctic Using a Satellite Imager and Implications for Observing Feedback Mechanisms, *J. Climate*, 23, 1894–1907, <https://doi.org/10.1175/2009JCLI3386.1>, 2010.
- Lüpkes, C., Ehrlich, A., Wendisch, M., Crewell, S., and Mech, M.: Master tracks in different resolutions during POLAR 5 campaign AFLUX 2019, Alfred Wegener Institute, Helmholtz Centre for Polar and Marine Research, Bremerhaven, PANGAEA [data set], <https://doi.org/10.1594/PANGAEA.902876>, 2019.
- Mayer, B. and Kylling, A.: Technical note: The libRadtran software package for radiative transfer calculations - description and examples of use, *Atmos. Chem. Phys.*, 5, 1855–1877, <https://doi.org/10.5194/acp-5-1855-2005>, 2005.
- McFarquhar, G. M., Zhang, G., Poellot, M. R., Kok, G. L., McCoy, R., Tooman, T., Fridlind, A., and Heymsfield, A. J.: Ice properties of single-layer stratocumulus during the Mixed-Phase Arctic Cloud Experiment: 1. Observations, *J. Geophys. Res.*, 112, D24201, <https://doi.org/10.1029/2007jd008633>, 2007.
- Mech, M., Kliesch, L.-L., Anhäuser, A., Rose, T., Kollias, P., and Crewell, S.: Microwave Radar/radiometer for Arctic Clouds (MiRAC): first insights from the ALOUD campaign, *Atmos. Meas. Tech.*, 12, 5019–5037, <https://doi.org/10.5194/amt-12-5019-2019>, 2019.
- Mech, M., Ehrlich, A., Herber, A., Lüpkes, C., Wendisch, M., Becker, S., Boose, Y., Chechin, D., Crewell, S., Dupuy, R., Gourbeyre, C., Hartmann, J., Jäkel, E., Jourdan, O., Kliesch, L.-L., Klingebiel, M., Kulla, B. S., Mioche, G., Moser, M., Risse, N., Donoso, E. R., Schäfer, M., Stapf, J., and Voigt, C.: MOSAiC-ACA and AFLUX – Arctic airborne campaigns characterizing the exit area of MOSAiC, *Sci. Data*, 9, 790, <https://doi.org/10.1038/s41597-022-01900-7>, 2022a.
- Mech, M., Risse, N., Crewell, S., and Kliesch, L.-L.: Radar reflectivities at 94 GHz and microwave brightness temperature measurements at 89 GHz during the AFLUX Arctic airborne cam-

- paign in spring 2019 out of Svalbard, PANGAEA [data set], <https://doi.org/10.1594/PANGAEA.944506>, 2022b.
- Mioche, G., Jourdan, O., Ceccaldi, M., and Delanoë, J.: Variability of mixed-phase clouds in the Arctic with a focus on the Svalbard region: a study based on spaceborne active remote sensing, *Atmos. Chem. Phys.*, 15, 2445–2461, <https://doi.org/10.5194/acp-15-2445-2015>, 2015.
- Moser, M. and Voigt, C.: DLR in-situ cloud measurements during AFLUX Arctic airborne campaign, PANGAEA [data set], <https://doi.org/10.1594/PANGAEA.940564>, 2022.
- Moser, M., Voigt, C., Jurkat-Witschas, T., Hahn, V., Mioche, G., Jourdan, O., Dupuy, R., Gourbeyre, C., Schwarzenboeck, A., Lucke, J., Boose, Y., Mech, M., Borrmann, S., Ehrlich, A., Herber, A., Lüpkes, C., and Wendisch, M.: Microphysical and thermodynamic phase analyses of Arctic low-level clouds measured above the sea ice and the open ocean in spring and summer, *Atmos. Chem. Phys.*, 23, 7257–7280, <https://doi.org/10.5194/acp-23-7257-2023>, 2023.
- Nakajima, T. and King, M. D.: Determination of the Optical Thickness and Effective Particle Radius of Clouds from Reflected Solar Radiation Measurements. Part I: Theory, *J. Atmos. Sci.*, 47, 1878–1893, [https://doi.org/10.1175/1520-0469\(1990\)047<1878:DOTOTA>2.0.CO;2](https://doi.org/10.1175/1520-0469(1990)047<1878:DOTOTA>2.0.CO;2), 1990.
- Platnick, S.: Vertical photon transport in cloud remote sensing problems, *J. Geophys. Res.-Atmos.*, 105, 22919–22935, <https://doi.org/10.1029/2000JD900333>, 2000.
- Platnick, S.: Approximations for horizontal photon transport in cloud remote sensing problems, *J. Quant. Spectrosc. Ra.*, 68, 75–99, [https://doi.org/10.1016/S0022-4073\(00\)00016-9](https://doi.org/10.1016/S0022-4073(00)00016-9), 2001.
- Platnick, S., Meyer, K. G., King, M. D., Wind, G., Amarasinghe, N., Marchant, B., Arnold, G. T., Zhang, Z., Hubanks, P. A., Holz, R. E., Yang, P., Ridgway, W. L., and Riedi, J.: The MODIS cloud optical and microphysical products: Collection 6 updates and examples from Terra and Aqua, *IEEE T. Geosci. Remote*, 55, 502–525, 2016.
- Rantanen, M., Karpechko, A. Y., Lipponen, A., Nordling, K., Hyvärinen, O., Ruosteenoja, K., Vihma, T., and Laaksonen, A.: The Arctic has warmed nearly four times faster than the globe since 1979, *Communications Earth & Environment*, 3, 168, <https://doi.org/10.1038/s43247-022-00498-3>, 2022.
- Rosenburg, S., Lange, C., Jäkel, E., Schäfer, M., Ehrlich, A., and Wendisch, M.: Retrieval of snow layer and melt pond properties on Arctic sea ice from airborne imaging spectrometer observations, *Atmos. Meas. Tech.*, 16, 3915–3930, <https://doi.org/10.5194/amt-16-3915-2023>, 2023.
- Ruiz-Donoso, E., Ehrlich, A., Schäfer, M., Jäkel, E., and Wendisch, M.: Spectral solar cloud top radiance measured by airborne spectral imaging during the ALOUD campaign in 2017, Leipzig Institute for Meteorology, University of Leipzig, PANGAEA [data set], <https://doi.org/10.1594/PANGAEA.902150>, 2019.
- Ruiz-Donoso, E., Ehrlich, A., Schäfer, M., Jäkel, E., Schemann, V., Crewell, S., Mech, M., Kulla, B. S., Kliesch, L.-L., Neuber, R., and Wendisch, M.: Small-scale structure of thermodynamic phase in Arctic mixed-phase clouds observed by airborne remote sensing during a cold air outbreak and a warm air advection event, *Atmos. Chem. Phys.*, 20, 5487–5511, <https://doi.org/10.5194/acp-20-5487-2020>, 2020.
- Schäfer, M., Bierwirth, E., Ehrlich, A., Heyner, F., and Wendisch, M.: Retrieval of cirrus optical thickness and assessment of ice crystal shape from ground-based imaging spectrometry, *Atmos. Meas. Tech.*, 6, 1855–1868, <https://doi.org/10.5194/amt-6-1855-2013>, 2013.
- Schäfer, M., Ruiz-Donoso, E., Ehrlich, A., and Wendisch, M.: Spectral solar cloud top and surface radiance measured by airborne spectral imaging during the AFLUX campaign in 2019, PANGAEA [data set], <https://doi.org/10.1594/PANGAEA.930932>, 2021.
- Serreze, M. C. and Barry, R. G.: Processes and impacts of Arctic amplification: A research synthesis, *Global Planet. Change*, 77, 85–96, <https://doi.org/10.1016/j.gloplacha.2011.03.004>, 2011.
- Serreze, M. C. and Francis, J. A.: The Arctic Amplification debate, *Climatic Change*, 76, 241–264, <https://doi.org/10.1007/s10584-005-9017-y>, 2006.
- Spreen, G., Kaleschke, L., and Heygster, G.: Sea ice remote sensing using AMSR-E 89-GHz channels, *J. Geophys. Res.-Oceans*, 113, C02S03, <https://doi.org/10.1029/2005JC003384>, 2008.
- Stamnes, K., Tsay, S.-C., Wiscombe, W., and Laszlo, I.: DISORT, a General-Purpose Fortran Program for Discrete-Ordinate-Method Radiative Transfer in Scattering and Emitting Layered Media: Documentation of Methodology, Tech. rep., Dept. of Physics and Engineering Physics, Stevens Institute of Technology, Hoboken, NJ 07030, <http://www.libradtran.org/lib/execute.php?media=disortreport1.1.pdf> (last access: 9 December 2023), 2000.
- Stroeve, J., Serreze, M., Holland, M., Kay, J., Malanik, J., and Barrett, A.: The Arctic's rapidly shrinking sea ice cover: A research synthesis, *Climatic Change*, 110, 1005–1027, <https://doi.org/10.1007/s10584-011-0101-1>, 2012.
- Tan, I. and Storelvmo, T.: Evidence of Strong Contributions From Mixed-Phase Clouds to Arctic Climate Change, *Geophys. Res. Lett.*, 46, 2894–2902, <https://doi.org/10.1029/2018GL081871>, 2019.
- Voigt, C., Schumann, U., Minikin, A., Abdelmonem, A., Afchine, A., Borrmann, S., Boettcher, M., Buchholz, B., Bugliaro, L., Costa, A., Curtius, J., Dollner, M., Dörnbrack, A., Dreiling, V., Ebert, V., Ehrlich, A., Fix, A., Forster, L., Frank, F., Fütterer, D., Giez, A., Graf, K., Groß, J.-U., Groß, S., Heimerl, K., Heinold, B., Hüneke, T., Järvinen, E., Jurkat, T., Kaufmann, S., Kennner, M., Klingebiel, M., Klimach, T., Kohl, R., Krämer, M., Krisna, T. C., Luebke, A., Mayer, B., Mertes, S., Molleker, S., Petzold, A., Pfeilsticker, K., Port, M., Rapp, M., Reutter, P., Rolf, C., Rose, D., Sauer, D., Schäfer, A., Schlage, R., Schnaiter, M., Schneider, J., Spelten, N., Spichtinger, P., Stock, P., Walser, A., Weigel, R., Weinzierl, B., Wendisch, M., Werner, F., Wernli, H., Wirth, M., Zahn, A., Ziereis, H., and Zöger, M.: ML-CIRRUS: The Airborne Experiment on Natural Cirrus and Contrail Cirrus with the High-Altitude Long-Range Research Aircraft HALO, *B. Am. Meteorol. Soc.*, 98, 271–288, <https://doi.org/10.1175/bams-d-15-00213.1>, 2017.
- Voigt, C., Lielieveld, J., Schlager, H., Schneider, J., Curtius, J., Meerkötter, R., Sauer, D., Bugliaro, L., Bohn, B., Crowley, J. N., Erbertseder, T., Groß, S., Hahn, V., Li, Q., Mertens, M., Pöhlker, M. L., Pozzer, A., Schumann, U., Tomsche, L., Williams, J., Zahn, A., Andreae, M., Borrmann, S., Bräuer, T., Dörich, R., Dörnbrack, A., Edtbauer, A., Ernle, L., Fischer, H., Giez, A., Granzin, M., Grewe, V., Harder, H., Heinritzi, M., Holanda, B. A., Jöckel, P., Kaiser, K., Krüger, O. O., Lucke, J., Marsing, A., Martin, A., Matthes, S., Pöhlker, C., Pöschl, U.,

- Reifenberg, S., Ringsdorf, A., Scheibe, M., Tadic, I., Zauner-Wieczorek, M., Henke, R., and Rapp, M.: Cleaner Skies during the COVID-19 Lockdown, *B. Am. Meteorol. Soc.*, 103, E1796–E1827, <https://doi.org/10.1175/bams-d-21-0012.1>, 2022.
- Wendisch, M. and Brenguier, J.-L.: *Airborne Measurements for Environmental Research – Methods and Instruments*, vol. 1, John Wiley & Sons, Ltd, ISBN 978-3-527-40996-9, 2013.
- Wendisch, M., Brückner, M., Burrows, J. P., Crewell, S., Dethloff, K., Ebell, K., Lüpkes, C., Macke, A., Notholt, J., Quaas, J., Rinke, A., and Tegen, I.: Understanding Causes and Effects of Rapid Warming in the Arctic, *EOS*, 98, <https://doi.org/10.1029/2017EO064803>, 2017.
- Wendisch, M., Macke, A., Ehrlich, A., Lüpkes, C., Mech, M., Chechin, D., Dethloff, K., Velasco, C. B., Bozem, H., Brückner, M., Clemen, H.-C., Crewell, S., Donth, T., Dupuy, R., Ebell, K., Egerer, U., Engelmann, R., Engler, C., Eppers, O., Gehrman, M., Gong, X., Gottschalk, M., Gourbeyre, C., Griesche, H., Hartmann, J., Hartmann, M., Heinold, B., Herber, A., Herrmann, H., Heygster, G., Hoor, P., Jafariserajehlou, S., Jäkel, E., Järvinen, E., Jourdan, O., Kästner, U., Kecorius, S., Knudsen, E. M., Köllner, F., Kretzschmar, J., Lelli, L., Leroy, D., Maturilli, M., Mei, L., Mertes, S., Mioche, G., Neuber, R., Nicolaus, M., Nomokonova, T., Notholt, J., Palm, M., van Pinxteren, M., Quaas, J., Richter, P., Ruiz-Donoso, E., Schäfer, M., Schmieder, K., Schnaiter, M., Schneider, J., Schwarzenböck, A., Seifert, P., Shupe, M. D., Siebert, H., Spreen, G., Stapf, J., Stratmann, F., Vogl, T., Welti, A., Wex, H., Wiedensohler, A., Zanatta, M., and Zeppenfeld, S.: The Arctic Cloud Puzzle: Using ALOUD/PASCAL Multiplatform Observations to Unravel the Role of Clouds and Aerosol Particles in Arctic Amplification, *B. Am. Meteorol. Soc.*, 100, 841–871, <https://doi.org/10.1175/BAMS-D-18-0072.1>, 2019.
- Wendisch, M., Brückner, M., Crewell, S., Ehrlich, A., Notholt, J., Lüpkes, C., Macke, A., Burrows, J. P., Rinke, A., Quaas, J., Maturilli, M., Schemann, V., Shupe, M. D., Akansu, E. F., Barrientos-Velasco, C., Bärfuss, K., Blechschmidt, A.-M., Block, K., Bougoudis, I., Bozem, H., Böckmann, C., Bracher, A., Bresson, H., Bretschneider, L., Buschmann, M., Chechin, D. G., Chylik, J., Dahlke, S., Deneke, H., Dethloff, K., Donth, T., Dorn, W., Dupuy, R., Ebell, K., Egerer, U., Engelmann, R., Eppers, O., Gerdes, R., Gierens, R., Gorodetskaya, I. V., Gottschalk, M., Griesche, H., Gryanik, V. M., Handorf, D., Harm-Altstädter, B., Hartmann, J., Hartmann, M., Heinold, B., Herber, A., Herrmann, H., Heygster, G., Höschel, I., Hofmann, Z., Hölemann, J., Hünerbein, A., Jafariserajehlou, S., Jäkel, E., Jacobi, C., Janout, M., Jansen, F., Jourdan, O., Jurányi, Z., Kalesse-Los, H., Kanzow, T., Käthner, R., Kliesch, L. L., Klingebiel, M., Knudsen, E. M., Kovács, T., Körtke, W., Krampe, D., Kretzschmar, J., Kreyling, D., Kulla, B., Kunkel, D., Lampert, A., Lauer, M., Lelli, L., von Lerber, A., Linke, O., Löhnert, U., Lonardi, M., Losa, S. N., Losch, M., Maahn, M., Mech, M., Mei, L., Mertes, S., Metzner, E., Mewes, D., Michaelis, J., Mioche, G., Moser, M., Nakoudi, K., Neggers, R., Neuber, R., Nomokonova, T., Oelker, J., Papakonstantinou-Presvelou, I., Pätzold, F., Pefanis, V., Pohl, C., van Pinxteren, M., Radovan, A., Rhein, M., Rex, M., Richter, A., Risse, N., Ritter, C., Rostosky, P., Rozanov, V. V., Donoso, E. R., Saavedra-Garfias, P., Salzmann, M., Schacht, J., Schäfer, M., Schneider, J., Schnierstein, N., Seifert, P., Seo, S., Siebert, H., Soppa, M. A., Spreen, G., Stachlewska, I. S., Stapf, J., Stratmann, F., Tegen, I., Viceto, C., Voigt, C., Vountas, M., Walbröl, A., Walter, M., Wehner, B., Wex, H., Willmes, S., Zanatta, M., and Zeppenfeld, S.: Atmospheric and Surface Processes, and Feedback Mechanisms Determining Arctic Amplification: A Review of First Results and Prospects of the (AC)3 Project, *B. Am. Meteorol. Soc.*, 104, E208–E242, <https://doi.org/10.1175/BAMS-D-21-0218.1>, 2022.
- Wendisch, M., Stapf, J., Becker, S., Ehrlich, A., Jäkel, E., Klingebiel, M., Lüpkes, C., Schäfer, M., and Shupe, M. D.: Effects of variable ice–ocean surface properties and air mass transformation on the Arctic radiative energy budget, *Atmos. Chem. Phys.*, 23, 9647–9667, <https://doi.org/10.5194/acp-23-9647-2023>, 2023.
- Werner, F., Siebert, H., Pilewskie, P., Schmeissner, T., Shaw, R. A., and Wendisch, M.: New airborne retrieval approach for trade wind cumulus properties under overlying cirrus, *J. Geophys. Res.-Atmos.*, 118, 3634–3649, <https://doi.org/10.1002/jgrd.50334>, 2013.
- Wesche, C., Steinhage, D., and Nixdorf, U.: Polar aircraft Polar 5 and Polar 6 operated by the Alfred Wegener Institute, *Journal of Large-Scale Research Facilities*, 2, A87, <https://doi.org/10.17815/jlsrf-2-153>, 2016.
- Zege, E., Katsev, I., Malinka, A., Prikhach, A., Heygster, G., and Wiebe, H.: Algorithm for retrieval of the effective snow grain size and pollution amount from satellite measurements, *Remote Sens. Environ.*, 115, 2674–2685, <https://doi.org/10.1016/j.rse.2011.06.001>, 2011.